

Unsupervised Material Fingerprinting: Ultra-fast hyperelastic model discovery from full-field experimental measurements

Moritz Flaschel^{a,1,*}, Miguel Angel Moreno-Mateos^{a,1,*}, Simon Wiesheier^{a,1}, Paul Steinmann^{a,c}, Ellen Kuhl^{a,b}

^a*Institute of Applied Mechanics, Friedrich-Alexander-Universität Erlangen-Nürnberg, Egerlandstr. 5, 91058, Erlangen, Germany*

^b*Department of Mechanical Engineering, 318 Campus Drive, Stanford University, California 94305, United States.*

^c*Glasgow Computational Engineering Centre, School of Engineering, University of Glasgow, G12 8QQ, United Kingdom*

Abstract

Material Fingerprinting is a lookup table-based strategy to discover material models from experimental measurements, which completely avoids the need to solve an optimization problem. In an offline phase, a comprehensive database of simulated material responses, so-called material fingerprints, is generated for a predefined experimental setup. This database can then be used repeatedly in the online phase to discover material models corresponding to experimentally measured observations. To this end, the experimentally measured fingerprint is compared with all fingerprints in the database to identify the closest match. The primary advantage of this strategy is that it does not require solving a continuous optimization problem. This avoids the associated computational costs as well as issues of ill-posedness caused by local minima in non-convex optimization landscapes. Material Fingerprinting has been successfully demonstrated for supervised datasets consisting of stress-strain pairs, as well as for unsupervised datasets involving full-field displacements and net reaction forces. However, to date, there is no experimental validation for the latter approach which is the objective of this work. Conventional unsupervised strategies to discover material models from full-field measurements can be broadly classified into methods that minimize the mismatch between measured and simulated displacements and methods that minimize the residuals of the weak formulation. The former is numerically robust but computationally expensive, while the latter is fast yet sensitive to noise due to the need to differentiate the measured displacement field. Unsupervised Material Fingerprinting offers a fast and robust alternative by directly comparing precomputed simulated displacements with measured data, which avoids both expensive optimization and sensitivity to noise. In this work, we apply this strategy to biaxial deformation tests of soft elastomer specimens with a central cut and inhomogeneity in the deformation field. To demonstrate the method's versatility and accuracy, we construct a single database for Material Fingerprinting across different materials and discover hyperelastic material models for Elastosil, Sylgard, and VHB tape. We show that, once the database is generated, Material Fingerprinting is several orders of magnitude faster than comparable optimization-based approaches for material model characterization from full-field measurements. The database generated in this work can be readily used to discover constitutive models for previously unseen materials by replicating the corresponding experimental protocols.

Keywords: material model discovery, pattern recognition, lookup table, database, experimental validation, full-field data

1. Introduction

“*Can Material Fingerprinting enable ultra-fast and robust material model discovery?*” This question has guided prior work on material model discovery (Flaschel et al., 2026). It now extends naturally to: “*Can unsupervised Material Fingerprinting robustly uncover hyperelastic behavior directly from real full-field experimental data?*”

Material modeling is fundamental to accurately capturing the constitutive response of a structure. While the identification of an appropriate strain energy density function was traditionally a trial-and-error process, recent advances

*Corresponding authors

Email addresses: moritz.flaschel@fau.de (Moritz Flaschel), miguel.moreno@fau.de (Miguel Angel Moreno-Mateos)

¹M. Flaschel, M. A. Moreno-Mateos, and S. Wiesheier contributed equally to this work.

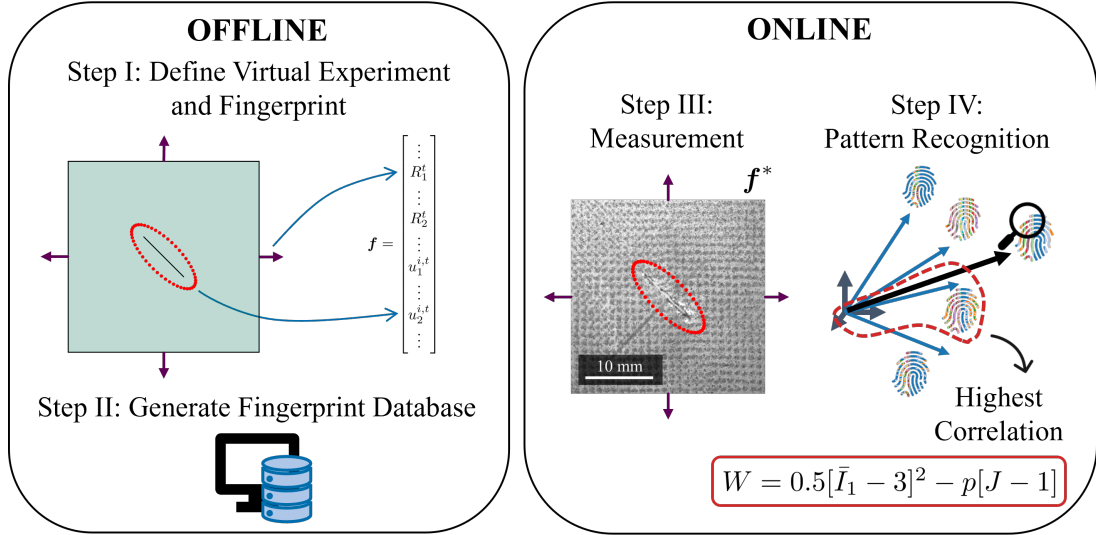


Figure 1: Schematic illustration of the unsupervised Material Fingerprinting workflow. In Step I, a standardized experiment is designed and the fingerprint vector is defined. In the unsupervised setting, the fingerprint incorporates both global reaction forces and local displacement measurements. In Step II, a database of fingerprints corresponding to different material models and parameter combinations is generated using finite element simulations. Once generated offline, this database can be reused indefinitely during the online stage. In Step III, the fingerprint of an unseen material is obtained experimentally. In Step IV, a pattern recognition algorithm is employed to discover the best-matching fingerprint in the database and, consequently, the corresponding material model.

in the material modeling community have led to a broad spectrum of methods for determining accurate constitutive descriptions and their parameters. In contrast to tests on simply shaped specimens with homogeneous deformation fields, modern material characterization methods rely on heterogeneous full-field experimental measurements of complexly shaped specimens (Avril et al., 2008; Pierron and Grédiac, 2020; Römer et al., 2025). As these methods rely on indirect, unlabeled data consisting of local displacements and global forces, in contrast to direct, labeled data consisting of stress-strain data pairs, we will refer to such methods as "unsupervised" in machine learning jargon. Among these methods, the Finite Element Model Updating (FEMU) approach is widely used for calibrating the parameters of constitutive models (cf. the seminal work in Collins et al. (1974) or more recent implementations in Wiesheier et al. (2024) and the framework DAVIS for data-adaptive Generalized Standard Materials Wiesheier et al. (2026)). FEMU consists of solving the boundary value problem with the Finite Element Method (FEM) to reproduce the experimental setup, while the material parameters are iteratively optimized to minimize a residual, typically defined from the mismatch between experimental and computational displacement fields and reaction forces. Its main strengths are its versatility and robustness, as it can provide a material law for virtually any boundary value problem that can be represented in a forward finite element simulation. However, FEMU can be computationally expensive and may show convergence issues in the optimization of the parameters due to the potential existence of multiple local minima in the optimization landscape. Another commonly adopted identification technique is to calibrate the material model parameters so that the residuals of the governing weak formulation are minimized. This strategy has been proposed as the Virtual Fields Method (VFM) (Grédiac, 1989; Grédiac and Vautrin, 1990; Grédiac et al., 2006) and the Equilibrium Gap Method (EGM) (Claire et al., 2004). An advancement of this strategy was subsequently used to automatically discover the optimal functional form of the material model through the EUCLID method (Efficient Unsupervised Constitutive Law Identification and Discovery) (Flaschel et al., 2021, 2022). These methods introduce experimentally measured displacement fields and reaction forces directly into the weak form of the governing equations and solve for the material parameters by enforcing equality (or near equality) between the internal and external virtual work. This strategy is computationally efficient because it does not require repeated solutions of boundary value problems. However, these approaches can be sensitive to noise, as the measured displacement fields must be differentiated to obtain strains, and they may lack robustness when the input displacement fields are incomplete.

Traditionally, material characterization relies on selecting a constitutive model a priori and identifying its parameters by fitting the model response to experimental observations. While effective in many cases, this paradigm has proven insufficient for capturing increasingly complex material behaviors. This limitation has spurred the development of data-driven and machine learning-based approaches to material characterization. In these methods, the constitutive response may be represented by flexible black-box models, including neural networks (Ghaboussi et al., 1991; As'ad and Farhat, 2022; Klein et al., 2022; Klein, 2025; Masi and Stefanou, 2023; Rosenkranz et al., 2023; Linden et al., 2023; Kalina et al., 2025; Flaschel et al., 2025c), spline-based representations (Sussman and

Bathe, 2009; Wiesheier et al., 2024; Geuken et al., 2025; Wiesheier et al., 2026), Gaussian processes (Frankel et al., 2020; Fuhr et al., 2022), neural ordinary differential equations (Tac et al., 2022), or parameterized non-smooth functions (Bleyer, 2025). More recent approaches leverage large language models for the generation of constitutive models (Tacke et al., 2025). Related approaches dispense with an explicit constitutive model altogether and instead perform simulations directly guided by experimental data (Kirchdoerfer and Ortiz, 2016; Ibañez et al., 2017). However, because purely data-driven and model-free strategies often lack physical interpretability, a complementary research direction has emerged that seeks to automatically infer interpretable constitutive models from data using symbolic or sparse regression techniques (Schoenauer et al., 1996; Flaschel et al., 2021, 2023, 2025a; Abdusalamov et al., 2023; Linka and Kuhl, 2023, 2024; Urrea-Quintero et al., 2026). Rather than tuning parameters within a prescribed model class, these methods aim to uncover both the functional form of the material law and its associated parameters directly from experimental observations. For a more comprehensive review of data-driven methods for constitutive modeling, we refer to Fuhr et al. (2024). However, a key limitation of existing data-driven approaches for material model learning and discovery is their reliance on optimization procedures, which are often computationally expensive and provide no guaranty of converging to the global optimum.

Very recently, a novel method termed Material Fingerprinting² has emerged as a fast, robust, and easy-to-implement approach for mechanical material characterization (Flaschel et al., 2026), see Fig. 1. The method leverages a pre-computed database in combination with a pattern recognition framework to determine the constitutive “fingerprint” of a given material. The central premise is that each material exhibits a unique fingerprint that characterizes its mechanical response in a predefined experiment. These fingerprints are generated offline through forward finite-element simulations of a prescribed boundary value problem. In a subsequent online phase, a pattern recognition algorithm identifies the database entry that best matches the experimentally measured fingerprint. This strategy offers several key advantages: it achieves exceptional computational efficiency, with the online identification stage completed within seconds. Moreover, Material Fingerprinting circumvents the need to solve a continuous optimization problem, which is often computationally expensive and prone to convergence issues, particularly in the presence of non-convex objective functions or nonlinear constraints. In contrast to approaches that calibrate the parameters of a preselected material model, Material Fingerprinting automatically discovers an interpretable and suitable functional form of the constitutive model. By restricting the database generation to physically admissible material models, the identified models are guaranteed to satisfy fundamental physical principles such as objectivity and thermodynamic consistency. Finally, the Material Fingerprinting framework is highly versatile and can be applied to a wide range of experimental setups and material behaviors. The method has been numerically verified for synthetically generated data from tests with homogeneous and heterogeneous deformation fields by Flaschel et al. (2026). A first experimental investigation by Martonová et al. (2026) validated the approach using tests with homogeneous strain fields. Building on this work, a pip-installable, open-source Python package for Material Fingerprinting, tailored to experiments with homogeneous strain fields, has been released (Flaschel et al., 2025b). However, experimental validation for tests with heterogeneous strain fields, i.e., unsupervised approach, remains an open question that this contribution aims to address.

In this contribution, we present the first application of unsupervised Material Fingerprinting to real experimental data consisting of full field measurements and reaction forces for the discovery of hyperelastic behavior in five distinct materials. A database of material fingerprints associated with incompressible hyperelastic constitutive models is generated in an offline phase using forward finite element simulations of a predefined biaxial test. The considered specimen geometry contains a central cut, which induces heterogeneous strain fields. Subsequently, in an online phase, a pattern recognition algorithm identifies the database fingerprint that best matches the experimentally measured fingerprint. The proposed methodology is validated using experimental data for three different grades of Elastosil, as well as Sylgard and VHB tape, which were previously acquired in the experimental study of Moreno-Mateos et al. (2025). The modus operandi of Material Fingerprinting is first demonstrated using a Cosine similarity based pattern recognition scheme introduced in earlier work (Flaschel et al., 2026). This similarity measure emphasizes the shape of the fingerprints while disregarding their absolute magnitudes. In the unsupervised setting considered here, each fingerprint incorporates multiple physical quantities, namely reaction forces and displacement fields, which makes it essential to retain information related to both shape and magnitude. For this reason, we introduce a novel similarity measure for pattern recognition based on a Euclidean metric. This metric has not previously been investigated within the Material Fingerprinting framework and is particularly well suited for the present application, as it preserves variations in magnitude as well as the geometric structure of the

²The term Material Fingerprinting is inspired by the Magnetic Resonance Fingerprinting (MRF) method by Ma et al. (2013), who proposed an inverse lookup table-driven strategy for quantitative magnetic resonance imaging, see also McGivney et al. (2014); Davies et al. (2014); Dong et al. (2025). Similar strategies have been proposed in the field of rheology by Rouze et al. (2018); Trutna et al. (2019, 2020a,b). We also note that the terms Fingerprinting and Material Fingerprinting have been used outside the domain of mechanics (Spannaus et al., 2021; Kuban et al., 2022; Filip et al., 2024; Jaafreh et al., 2025).

fingerprints.

In this study, the material fingerprints database is generated according to a predefined experimental protocol that is designed to be reproducible across a wide range of materials across laboratories. It is important to note that any database used for Material Fingerprinting is inherently tied to a fixed experimental configuration, including both specimen geometry and loading conditions. Consequently, any modification to the experimental setup necessitates the generation of a new database. While this requirement represents a limitation of the approach, reliance on standardized testing protocols for material characterization is both reasonable and well established in the literature. Analogous to existing technical standards that prescribe specific specimen geometries, such as dog-bone samples, the Material Fingerprinting framework envisions databases that are accompanied by clearly defined experimental guidelines specifying the required sample geometry and loading conditions to ensure consistency with the database. Furthermore, supplementary files for the three-dimensional printing of molds required for in-house specimen fabrication could be provided as part of a dedicated Material Fingerprinting handbook. Once such experimental guidelines are established and a comprehensive database is generated and made publicly available, unsupervised material characterization via Material Fingerprinting becomes highly efficient and robust.

2. Material Fingerprinting

In our earlier work, we introduced Material Fingerprinting, a database-driven approach for the rapid discovery of material models from either supervised or unsupervised experiments (Flaschel et al., 2026). In this work, we focus on the unsupervised setting, in which local displacement data over the specimen surface and global reaction forces at the specimen boundary are available, but no local stress measurements are provided. Because different materials produce distinct displacement and force responses, a vector containing both quantities can be interpreted as the material’s fingerprint. To enable model discovery, we first construct a database of simulated fingerprints for a wide range of material models and parameter combinations using finite element simulations. Combined with an appropriate pattern recognition algorithm, this database can then be queried repeatedly to identify suitable material models and their parameters for previously unseen materials. In the following, we describe the standardized experiment, the definition of the fingerprints, the database generation procedure, and the pattern recognition framework underlying Material Fingerprinting, which we later apply to discover material models from experimentally measured fingerprints.

2.1. Standardized experiment

As described previously, our experimental tests follow a standardized procedure: all experimentally tested specimens share the same geometry, and identical loading conditions are applied. For the database generation, we consider a biaxial test of a thin specimen with a central notch to introduce heterogeneity in the strain field, as illustrated in Fig. 2. The side length of the square specimen measures 85 mm, and a thickness of 2 mm is assumed. As discussed later, the specimen is assumed to be sufficiently thin such that the reaction forces scale linearly with specimen thickness for fixed applied displacements. The notch is oriented at 45° with respect to the loading axes and has a length of 10 mm. We apply an equibiaxial displacement of 29.75 mm over 35 equidistant steps, at which reaction forces and displacements can be recorded. We chose this predefined experimental protocol such that it can be reproduced experimentally for different materials across laboratories.

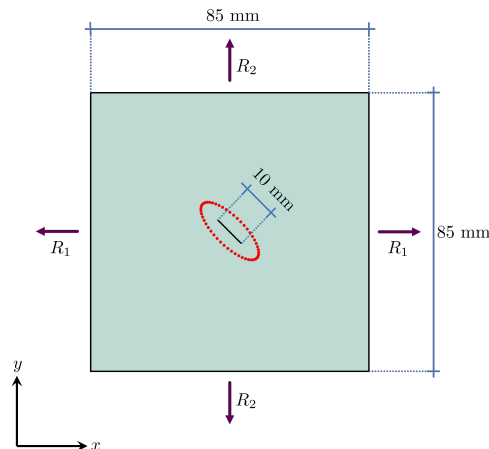


Figure 2: Illustration of the standardized experimental setup. The specimen is under biaxial tension. The global reaction forces can be measured via load cells and the displacements at the red markers can be measured using full-field measurement or local point tracking techniques.

2.2. Fingerprint definition

In the following, we define the material fingerprint tailored to the aforementioned fixed experimental conditions. Specifically, a fingerprint is a real-valued vector \mathbf{f} that contains both the forces and displacements resulting from the applied deformation. Therefore, a fingerprint encodes the characteristic mechanical response of the material. During the experiment, the reaction forces measured for each axis at the specimen boundary across a predefined set of load steps are collected in a vector $\mathbf{f}_R \in \mathbb{R}^{2n_t}$, where n_t denotes the number of load steps. Two reaction forces, which are obtained from the equibiaxial experiments reported in [Moreno-Mateos et al. \(2025\)](#), correspond to the measured forces along the two independent loading axes. Experimental variability, such as inconsistencies introduced during sample fabrication or during mounting on the biaxial testing machine, results in the two reaction forces not being exactly identical (see [Section 3](#) for further details). Alternatively, the fingerprints could be defined using averaged reaction forces.

Likewise, the displacements measured at a predefined set of surface points are assembled into a vector $\mathbf{f}_u \in \mathbb{R}^{2n_u n_t}$, where n_u is the number of surface points contributing to the fingerprint. [Fig. 2](#) illustrates the surface points selected for constructing the fingerprint. Because the deformation field exhibits the greatest variation near the central crack, we place the measurement points along an ellipse surrounding this region. At the same time, full-field measurements tend to be less reliable near specimen boundaries, so the ellipse is chosen with a sufficient radius to maintain a buffer zone between the notch and the measurement points. The reaction forces and displacements are concatenated into the fingerprint vector $\mathbf{f} = [\mathbf{f}_R; \mathbf{f}_u] \in \mathbb{R}^{n_f}$ with $n_f = 2n_t + 2n_u n_t$. Here, we note that the order in which the measurements appear in the fingerprint vector is irrelevant, provided that this ordering is applied consistently throughout all simulations and experiments.

2.3. Database generation

To generate a database of material fingerprints, we virtually reproduce the standardized experimental setup described in [Section 2.1](#) and simulate its response using three-dimensional finite element computations for a predefined set of material models and parameter combinations. In this work, we focus on incompressible and isotropic materials for which the material behavior is characterized by the strain energy density function

$$W(\mathbf{F}; \boldsymbol{\theta}, \boldsymbol{\alpha}) = \tilde{W}(\mathbf{F}; \boldsymbol{\theta}, \boldsymbol{\alpha}) - p[J - 1], \quad (1)$$

where $\mathbf{F} = \nabla_0 \mathbf{u} + \mathbf{I}$ is the deformation gradient of the displacement field \mathbf{u} , with \mathbf{I} the second-order identity tensor, p is a Lagrange multiplier enforcing the incompressibility constraint $J = \det(\mathbf{F}) = 1$, $\boldsymbol{\theta}$ is a vector of homogeneity material parameters while $\boldsymbol{\alpha}$ is a vector of non-homogeneity material parameters (the difference between the two last ones will be explained in [Section 2.4](#)). For isotropic materials, the isochoric strain energy density \tilde{W} may be a function of the invariants \bar{I}_1, \bar{I}_2 or the principal stretches $\lambda_1, \lambda_2, \lambda_3$. Specifically, we have $\bar{I}_1 = J^{-2/3} I_1$ and $\bar{I}_2 = J^{-4/3} I_2$, where $I_1 = \text{tr}(\mathbf{C})$ and $I_2 = \frac{1}{2}[\text{tr}(\mathbf{C}^2) - \text{tr}(\mathbf{C}^2)]$ are the first and second invariants of the right Cauchy-Green tensor $\mathbf{C} = \mathbf{F}^T \cdot \mathbf{F}$, and $\lambda_1, \lambda_2, \lambda_3$ are the square roots of the eigenvalues of \mathbf{C} .

We consider seven incompressible hyperelastic material models: the Carroll model ([Carroll, 2011](#)), the Lopez-Pamies model ([Lopez-Pamies, 2009](#)), the Mooney-Rivlin model ([Rivlin, 1950](#)), the Neo-Hookean model ([Treloar, 1944](#)), the generalized Neo-Hookean model ([Stephenson, 1982; Geubelle and Knauss, 1994](#)), the Ogden model ([Ogden, 1972](#)), and the Yeoh model ([Yeoh, 1990](#)). For each model, we perform multiple simulations across a range of parameter values and store the resulting fingerprints, together with the corresponding model metadata, in the database. [Table 1](#) summarizes the material models, their strain energy density functions, and the parameter ranges used during database generation. Each simulation results in a fingerprint vector $\mathbf{f}^{(i)}$ with $i = 1, \dots, n_d$, where n_d denotes the number of fingerprints in the database. The finite element simulations are implemented in the open-source finite element platform FEniCSx. Details about the implementation are provided in [Appendix A](#).

For the database generation, the number of load steps n_t is chosen to be sufficiently large to span the entire elastic regime up to the onset of crack propagation for all experiments. Selecting a sufficiently large n_t ensures that the database remains applicable to future experiments, even when the exact load step at which crack propagation will occur cannot be anticipated. We note that incompressible finite element simulations may suffer from convergence issues, particularly at larger load steps or for material models exhibiting strong nonlinearities. During database generation, if a simulation fails to converge at a given load step, we set all fingerprint entries for that load step and all subsequent load steps to zero. As a result, the fingerprint is no longer usable across the full load range but remains valid for experimental data restricted to the lower load regime.

2.4. Homogeneity property

The material parameters directly influence the resultant forces and displacements in the finite element simulations. We distinguish between so-called homogeneity parameters $\boldsymbol{\theta}$ and non-homogeneity parameters $\boldsymbol{\alpha}$ ([Flaschel](#)

Table 1: Material models and parameter combinations considered during database generation.

Models	Strain energy density \tilde{W}	Parameters ranges	# Fingerprints
Carroll	$\theta_1 \bar{I}_1 + \theta_2 \bar{I}_1^4 + \theta_3 \sqrt{\bar{I}_2}$	$\theta_1 = 1.0, \theta_2 \in [0.1, 10.0], \theta_3 \in [0.1, 10.0]$	100
Lopez-Pamies	$\theta_4 [\bar{I}_1^{\alpha_1} - 3^{\alpha_1}]$	$\theta_4 = 1.0, \alpha_1 \in [0.01, 10.0]$	100
Mooney-Rivlin	$\theta_5 [\bar{I}_1 - 3] + \theta_6 [\bar{I}_2 - 3]$	$\theta_5 = 1.0, \theta_6 \in [0.1, 10.0]$	100
Neo-Hookean	$\theta_5 [\bar{I}_1 - 3]$	$\theta_5 = 1.0$	1
Gen. Neo-Hookean	$\theta_7 \left[\left[1 + \alpha_2 [\bar{I}_1 - 3] \right]^{\alpha_3} - 1 \right]$	$\theta_7 = 1.0, \alpha_2 \in [0.01, 10.0], \alpha_3 \in [0.5, 10.0]$	400
Ogden	$\theta_8 [\lambda_1^{\alpha_4} + \lambda_2^{\alpha_4} + \lambda_3^{\alpha_4} - 3]$	$\theta_8 = 1.0, \alpha_4 \in [1.0, 10.0]$	100
Yeoh	$\theta_5 [\bar{I}_1 - 3] + \theta_9 [\bar{I}_1 - 3]^2 + \theta_{10} [\bar{I}_1 - 3]^3$	$\theta_5 = 1.0, \theta_9 \in [0.1, 10.0], \theta_{10} \in [0.1, 10.0]$	100
			$n_d = 901$

et al., 2026), such that the isochoric strain energy density functions can be written as a linear combination of the homogeneity parameters and functions \mathbf{Q} of the deformation and the non-homogeneity parameters

$$\tilde{W}(\mathbf{F}; \boldsymbol{\theta}, \boldsymbol{\alpha}) = \boldsymbol{\theta} \cdot \mathbf{Q}(\mathbf{F}; \boldsymbol{\alpha}). \quad (2)$$

When the finite element analysis is performed under pure displacement control, multiplying the strain energy density by a factor scales the reaction forces proportionally, while the displacement field remains unaffected. Specifically, the forces obey the homogeneity relation $\mathbf{f}_R^{(i)}(a\boldsymbol{\theta}, \boldsymbol{\alpha}) = a\mathbf{f}_R^{(i)}(\boldsymbol{\theta}, \boldsymbol{\alpha})$, $\forall a \in \mathbb{R}$, whereas the displacements remain unchanged under such scaling $\mathbf{f}_u^{(i)}(a\boldsymbol{\theta}, \boldsymbol{\alpha}) = \mathbf{f}_u^{(i)}(\boldsymbol{\theta}, \boldsymbol{\alpha})$, $\forall a \in \mathbb{R}$. These relations are useful because, after the pattern recognition algorithm identifies the material model, they allow the homogeneity parameters $\boldsymbol{\theta}$ to be properly scaled to match the observed forces. We note that the functional form in Eq. (2) imposes no restrictions on hyperelastic material models because the functions \mathbf{Q} may depend nonlinearly on the parameters $\boldsymbol{\alpha}$, and that all models in the literature fall within this form (Dal et al., 2021).

2.5. Pattern recognition algorithm with Cosine similarity

After generating the database, it can be leveraged repeatedly for material model discovery. To this end, the standardized experiment must be conducted for the material under consideration, and the material's fingerprint must be measured. In the following, we denote the experimentally measured fingerprint by \mathbf{f}^* . We note, however, that it is not always possible to acquire data for all load steps n_f experimentally, as the material may fail before reaching the final load step. Thus, it might not always be possible to acquire the entire fingerprint. In this case, a reduced fingerprint $\hat{\mathbf{f}}^* \in \mathbb{R}^{\hat{n}_f}$ with $\hat{n}_f < n_f$ is measured and used for Material Fingerprinting by loading only the corresponding reduced fingerprints $\hat{\mathbf{f}}^{(i)}$ from the database.

Given an experimentally measured fingerprint $\hat{\mathbf{f}}^*$, the Material Fingerprinting method discovers a suitable material model by searching the database for the best matching fingerprint $\hat{\mathbf{f}}^{(i)}$. To this end, the measured fingerprint and the fingerprints in the database are normalized

$$\bar{\mathbf{f}}_R^* = \frac{\hat{\mathbf{f}}_R^*}{\|\hat{\mathbf{f}}_R^*\|}, \bar{\mathbf{f}}_u^* = \frac{\hat{\mathbf{f}}_u^*}{\|\hat{\mathbf{f}}_u^*\|}, \bar{\mathbf{f}}_R^{(i)} = \frac{\hat{\mathbf{f}}_R^{(i)}}{\|\hat{\mathbf{f}}_R^{(i)}\|}, \bar{\mathbf{f}}_u^{(i)} = \frac{\hat{\mathbf{f}}_u^{(i)}}{\|\hat{\mathbf{f}}_u^{(i)}\|}. \quad (3)$$

Due to normalization, the inner products of the fingerprints are equal to the cosines of the angles between the fingerprints

$$\cos(\beta_R^{(i)}) = \bar{\mathbf{f}}_R^{(i)} \cdot \bar{\mathbf{f}}_R^*, \cos(\beta_u^{(i)}) = \bar{\mathbf{f}}_u^{(i)} \cdot \bar{\mathbf{f}}_u^*, \quad (4)$$

where $\beta_R^{(i)}$ is the angle between $\hat{\mathbf{f}}_R^{(i)}$ and $\hat{\mathbf{f}}_R^*$, and $\beta_u^{(i)}$ is the angle between $\hat{\mathbf{f}}_u^{(i)}$ and $\hat{\mathbf{f}}_u^*$. Hence, the inner products are also called Cosine similarities. Because the inverse cosines $\cos^{-1}(\square)$ are monotonically decreasing functions for $\square \in [-1, 1]$, the Cosine similarities are inversely proportional to the angles between the fingerprints.

We finally identify the fingerprint in the database with the highest agreement with the experimentally measured data. To this end, we seek the maximum of a weighted measure between the Cosine similarities of the reaction and displacement fingerprints

$$i_C^* = \arg \max_{i=1, \dots, n_d} \left[\frac{1}{n_{f_R}} \cos(\beta_R^{(i)}) + \frac{1}{n_{f_u}} \cos(\beta_u^{(i)}) \right], \quad (5)$$

where n_{f_R} and n_{f_u} denote the dimensions of the fingerprints $\bar{\mathbf{f}}_R^*$ and $\bar{\mathbf{f}}_u^*$, respectively. In contrast to a continuous optimization problem, finding the maximum over a set of discrete values is orders of magnitude more computationally efficient.

The reader might note that the normalization in [Eq. \(3\)](#) serves to place the reaction force and displacement contributions on a comparable scale. Both contribute equally to the recognition algorithm in [Eq. \(5\)](#), ensuring that neither dominates the combined measure. In principle, we can adjust the relative impact of the reaction forces and displacements by introducing weights into the similarity measure. However, our numerical experiments indicate that our chosen measure of similarity consistently yields appropriate and robust results.

We finally obtain the discovered material model by rescaling the homogeneity parameters with the norm of the force measurements

$$\boldsymbol{\theta}^* = \|\tilde{\mathbf{f}}_R^*\| \bar{\boldsymbol{\theta}}^{(i_C^*)} \quad \text{and} \quad \boldsymbol{\alpha}^* = \boldsymbol{\alpha}^{(i_C^*)}. \quad (6)$$

2.6. Pattern recognition algorithm with Euclidean similarity

The cosine-similarity-based measure introduced in the previous section enables fingerprint recognition by primarily emphasizing the shape of the fingerprints. However, since the reaction forces and displacements concatenated into a fingerprint are normalized (cf. [Eq. \(3\)](#)), the proportionality between forces and displacements is not preserved. This motivates an alternative similarity measure based on Euclidean distance. Specifically, we define a second similarity metric using the Euclidean norm of the difference between the database and experimental reaction forces and displacements as

$$i_E^* = \arg \max_{i=1, \dots, n_d} \left[-\frac{\|\tilde{\mathbf{f}}_R^{(i)} - \tilde{\mathbf{f}}_R^*\|^2}{\|\tilde{\mathbf{f}}_R^*\|^2} - \frac{\|\tilde{\mathbf{f}}_u^{(i)} - \hat{\mathbf{f}}_u^*\|^2}{\|\hat{\mathbf{f}}_u^*\|^2} \right]. \quad (7)$$

The first term in [Eq. \(7\)](#) involves normalized force fingerprints. The use of the normalized vectors $\tilde{\mathbf{f}}_R^{(i)}$ and $\tilde{\mathbf{f}}_R^*$ with $\|\tilde{\mathbf{f}}_R^{(i)}\| = \|\tilde{\mathbf{f}}_R^*\| = 1$ is motivated by the homogeneity property of the strain energy density function. The homogeneity property described in [Section 2.4](#) leads to a proportional scaling of the reaction forces under a uniform scaling of the strain energy density function. Thus, it is sufficient to compare the relative shapes of the force fingerprints during pattern recognition and to determine the correct the magnitude of the strain energy density function in a subsequent postprocessing step. The displacement field remains invariant under a uniform scaling of the strain energy density function. Thus, the second term of the Euclidean similarity measure involves the non-normalized displacement fingerprints $\tilde{\mathbf{f}}_u^{(i)}$ and $\hat{\mathbf{f}}_u^*$. Here, the squared norm of the difference between the measured fingerprint and each fingerprint in the database is divided by the squared norm of the experimental fingerprint to obtain a nondimensional measure of similarity. The pattern recognition algorithm in [Eq. \(7\)](#) is reformulated as a maximization problem by changing the sign of the error norms such that the resulting term can be interpreted as a measure of similarity.

We emphasize that the quantity maximized in [Eq. \(7\)](#) is similar – but not identical – to the objective function typically minimized in parameter identification with the FEMU method. In FEMU, the goal is to minimize the absolute differences between measured and simulated reaction forces. In contrast, our approach minimizes the discrepancy between normalized reaction force fingerprint vectors. Consequently, we focus solely on the direction of the reaction force fingerprint vectors while disregarding their magnitudes. This is justified in the Material Fingerprinting context, as the correct force magnitudes can be recovered later during the rescaling of the homogeneity parameters. After identifying i_E^* , the rescaling of the homogeneity parameters is analogous to [Eq. \(6\)](#).

3. Experimental data

In this work, we validate the proposed Material Fingerprinting approach using the experimental data reported by the authors in [Moreno-Mateos et al. \(2025\)](#) under biaxial loading conditions. The campaign was carried out on standardized square samples made from five different soft materials (shear modulus below 250 kPa). Four of the materials were synthesized by curing two-component blends at elevated temperature: Elastosil P7670 at three volume mixing ratios (2:1, 8:5, and 1:1, ranging from softest to stiffest) and Sylgard 184 at the standard 10:1 ratio. All samples had a thickness of 2 mm; while the fifth material was VHB 4905 tape, supplied by the manufacturer as pre-formed sheets of thickness 0.5 mm. In addition, a notch in the middle maximizes the deformation heterogeneity. The notch is oriented at 45° with respect to the loading axes and has a length of 10 mm (cf. [Fig. 3a-b](#)). Equibiaxial tests under monotonic loading were performed at a quasi-static displacement rate of 0.85 mm s⁻¹ along each axis, starting from an initial clamp separation of 85 mm. Throughout the tests, 2D Digital Image Correlation (DIC) was applied to images captured during deformation and after crack propagation. In this work, however, we restrict our analysis to the displacement fields measured at loading steps preceding fracture initiation. The fingerprints are constructed as the geometric mean across four experimental repetitions. Details regarding the experimental fingerprint measurement are provided in [Appendix B](#).

We note that the experimental dataset provides a sufficiently dense set of load steps such that we can extract the fingerprint information at the load steps predefined in [Section 2.1](#). The experimental displacement field is sampled at nodes lying on an elliptic contour, as illustrated in [Fig. 3b-c](#) for both a representative sample and the finite element mesh used to generate the fingerprint database. This is possible due to the high spatial resolution of the experimental displacement fields obtained through DIC, which are originally computed on a square grid that is significantly denser than the set of points required for fingerprint construction.

Importantly, the experimental dataset is standardized with respect to both loading conditions and sample geometry. In this regard, it is noteworthy mentioning that VHB tape samples have a smaller thickness due to fabrication constraints. To account for the geometric discrepancy relative to the other four materials, the reaction forces in the experimental dataset for VHB tape are scaled by a factor of four, reflecting that its thickness is one quarter of the thickness of the virtual sample used to generate the database. This scaling is justified by an independent validation study in which forward simulations were performed for both the database thickness and the reduced VHB tape thickness, demonstrating that the resulting force-displacement curves scale almost perfectly linearly with thickness and that the deformation fields barely vary.

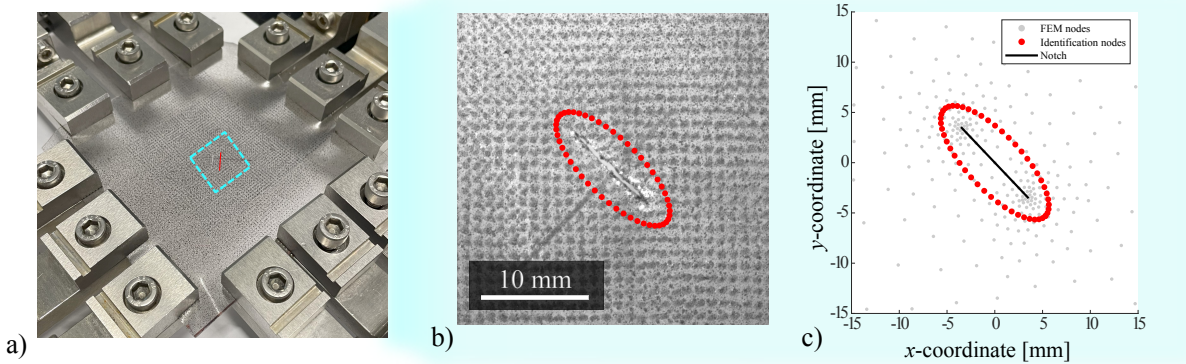


Figure 3: Experimental fingerprint measurement. (a) Experimental setup for the equibiaxial tests in [Moreno-Mateos et al. \(2025\)](#). (b) Close-up view of the strain concentrator (notch) and its vicinity. The points used to construct the fingerprints are marked in red color. (c) Close-up view of computational counterpart of the notch and points used to construct the fingerprints in the database.

4. Results and discussion

We apply Material Fingerprinting to the experimental data from the five materials described in [Section 3](#), using a single fingerprint database throughout the study, as discussed in [Section 2.3](#). We first present the results obtained using Cosine similarity for pattern recognition, and then discuss the results obtained with the newly proposed Euclidean similarity measure.

4.1. Cosine similarity

To illustrate the inner workings of Material Fingerprinting, and in particular the pattern recognition based on Cosine similarity, we show in [Fig. 4](#) the Cosine similarity computed for all fingerprints in the database. The computed Cosine similarities are ordered by magnitude, such that the most suitable fingerprint appears on the left. These plots highlight that multiple fingerprints in the database can yield similar similarity values, indicating that several models and combinations of material parameters are comparably capable of describing the data. This behavior is expected, as some models in the database can be viewed as generalizations of others, as is the case for the Neo-Hookean, generalized Neo-Hookean, and Ogden models. We observe that, particularly for Sylgard, many models exhibit similar Cosine similarity values. This is reasonable because, as shown later, the material response of Sylgard is close to linear under the experimental conditions.

To further illustrate the pattern recognition algorithm based on Cosine similarity, we present in [Fig. 5](#) the measured normalized fingerprints together with the best-matching normalized fingerprints from the database. The vectors are shown as graphs, with the vector index on the horizontal axis and the corresponding vector entries on the vertical axis. The left entries correspond to forces, and the right entries correspond to displacements in the fingerprint vectors. We observe a high level of agreement between the measured and identified fingerprints.

The pattern recognition algorithm identifies the Mooney–Rivlin model for the three Elastosil variants, the generalized Neo-Hookean model the Sylgard, and the Lopez-Pamies model for VHB tape as the most suitable models.

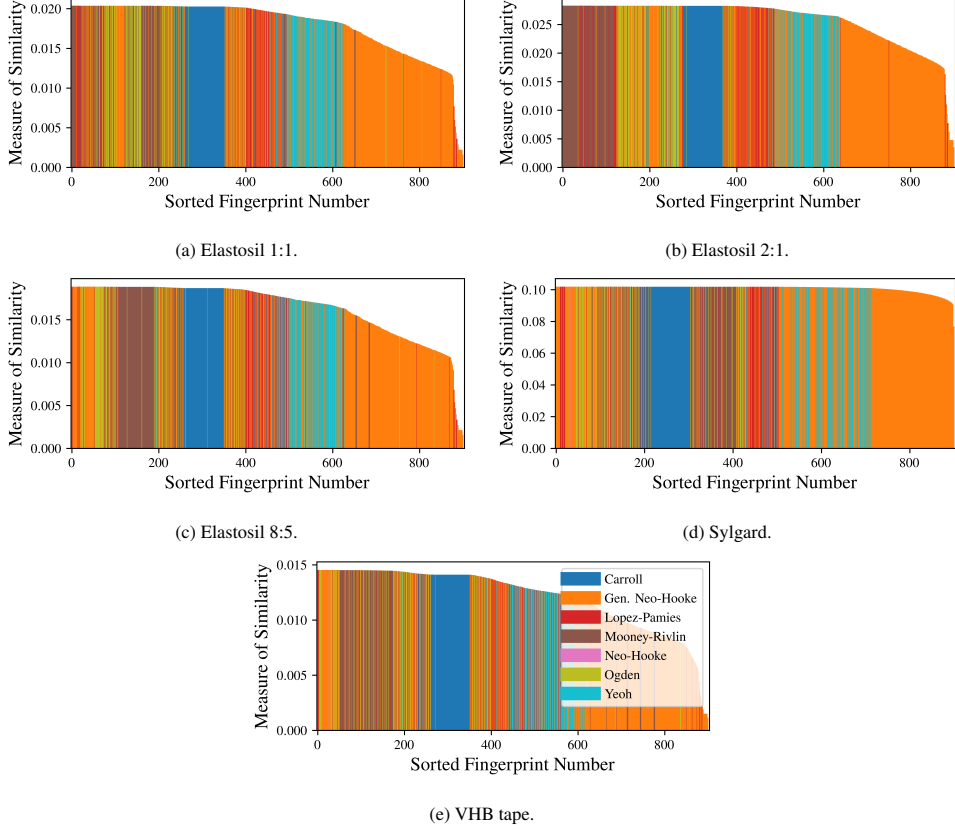


Figure 4: Illustration of the pattern recognition algorithm for Material Fingerprinting based on Cosine similarity. The plots displays the similarity measures for all fingerprints, sorted in descending order.

Table 2: Discovered strain energy density functions for Material Fingerprinting based on Cosine similarity.

Materials	Discovered Models	Strain Energy Density Functions \tilde{W} [N mm^{-2}]
Elastosil 1:1	Mooney-Rivlin	$0.0220[\bar{I}_1 - 3] + 0.0110[\bar{I}_2 - 3]$
Elastosil 2:1	Mooney-Rivlin	$0.0020[\bar{I}_1 - 3] + 0.0023[\bar{I}_2 - 3]$
Elastosil 8:5	Mooney-Rivlin	$0.0119[\bar{I}_1 - 3] + 0.0012[\bar{I}_2 - 3]$
Sylgard	Gen. Neo-Hookean	$0.1850 \left[\left[1 + 3.1647[\bar{I}_1 - 3] \right]^{0.5} - 1 \right]$
VHB tape	Lopez-Pamies	$0.0590[\bar{I}_1^{0.7164} - 3^{0.7164}]$

Interestingly, we uncover the same material model for all Elastosil variants where only the parameters vary. The discovered material models, strain energy density functions, and identified parameters are summarized in [Table 3](#).

For the Elastosil variants, the homogeneity parameter associated with the first invariant is consistently larger than the parameter associated with the second invariant. Hence, these models can be interpreted as \bar{I}_1 -dominated, similar to the spline-based energy functions calibrated previously by the authors [Moreno-Mateos et al. \(2025\)](#).

To assess the fitting accuracy of the model discovered by Material Fingerprinting, we compare the measured reaction forces and displacements to those predicted by the models in [Table 3](#). [Fig. 6](#) shows the experimentally measured and discovered reaction forces in the horizontal and vertical directions. For each clamp loading stage, the experimental reaction forces across the four repetitions were aggregated using the geometric mean. Overall, the reaction forces predicted by the discovered models agree well with the experimental scatter. As stated earlier, we observe an almost linear response for Sylgard, which explains why many models exhibit nearly identical Cosine similarity values in this case, see [Fig. 4](#).

[Fig. 7](#) shows the experimentally measured (a) and discovered (b) displacement fields. Analogous to the reaction forces, the experimental displacement fields for each clamp loading stage were also aggregated using the geometric

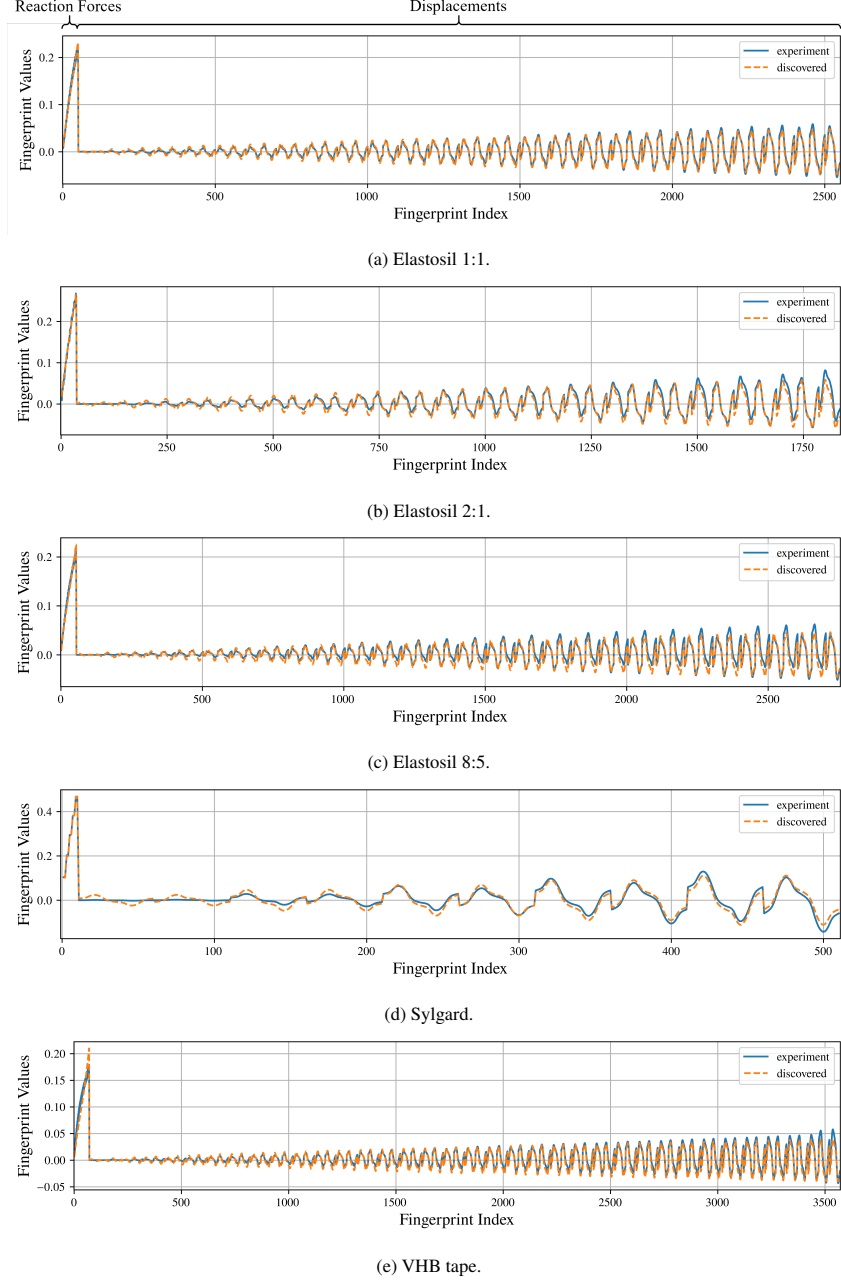


Figure 5: Comparison of the measured normalized fingerprints and the best-matching normalized fingerprints in the database for Material Fingerprinting based on Cosine similarity. Continuous curves are shown for visualization purposes only. In practice, the fingerprints consist of discrete vector entries. The fingerprint index has no physical meaning and is used solely to enable plotting and comparison of the experimental and database fingerprints.

mean. While reaction forces are shown for the entire range before crack onset, the displacement fields are presented only for the clamp loading stage at crack onset: 29.75 mm for VHB tape, 4.25 mm for Sylgard, 15.30 mm for Elastosil 2:1, 22.95 mm for Elastosil 8:5, and 21.25 mm for Elastosil 1:1. The error metric shown in Fig. 7c corresponds to the absolute error, normalized by the respective clamp loading stages listed above. The contour plots are restricted to a $20\text{ mm} \times 20\text{ mm}$ box surrounding the initial notch. Overall, the resulting errors remain small; however, some local disagreement between experiment and model is observed. This is expected, as the Cosine similarity metric used for model discovery primarily emphasizes the agreement of displacement directions rather than their absolute magnitude.

4.2. Euclidean similarity

As already mentioned, using Cosine similarity for pattern recognition in unsupervised Material Fingerprinting does not account for the magnitudes of the displacement fingerprints. Therefore, we introduce the Euclidean similarity

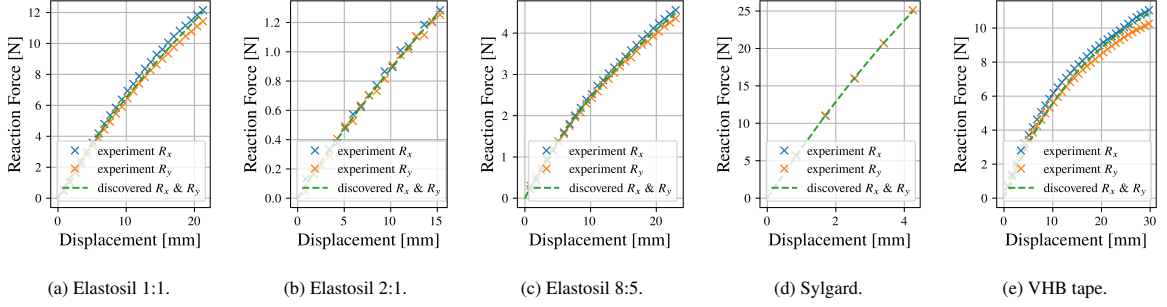


Figure 6: Comparison of the measured reaction forces and the reaction forces predicted by the discovered material models for Material Fingerprinting based on Cosine similarity. The two reaction forces R_x and R_y are obtained from the equibiaxial experiments in [Moreno-Mateos et al. \(2025\)](#) as the measured forces on each of the two independent axes. Due to experimental variability, the two reaction forces are not exactly identical.

in [Eq. \(7\)](#) as an alternative similarity measure. In the following, we discuss the results obtained with Material Fingerprinting based on Euclidean similarity.

[Table 3](#) summarizes the discovered models, their strain energy density functions, and the calibrated material parameters. For the three variants of Elastosil as well as for Sylgard, the Ogden model is identified. Consistent with the results obtained using Cosine similarity, the same model is discovered for all Elastosil variants, albeit with different material parameters. For the VHB tape, the generalized Neo-Hookean model is identified.

Table 3: Discovered strain energy density functions for Material Fingerprinting based on Euclidean similarity.

Materials	Discovered Models	Strain Energy Density Functions \tilde{W} [N mm^{-2}]
Elastosil 1:1	Ogden	$0.0218[\lambda_1^{2.6364} + \lambda_2^{2.6364} + \lambda_3^{2.6364} - 3]$
Elastosil 2:1	Ogden	$0.0015[\lambda_1^{3.7273} + \lambda_2^{3.7273} + \lambda_3^{3.7273} - 3]$
Elastosil 8:5	Ogden	$0.0074[\lambda_1^{2.7273} + \lambda_2^{2.7273} + \lambda_3^{2.7273} - 3]$
Sylgard	Ogden	$0.0125[\lambda_1^{10.0} + \lambda_2^{10.0} + \lambda_3^{10.0} - 3]$
VHB tape	Gen. Neo-Hookean	$5.9155 \left[\left[1 + 0.01[\bar{I}_1 - 3] \right]^{0.5} - 1 \right]$

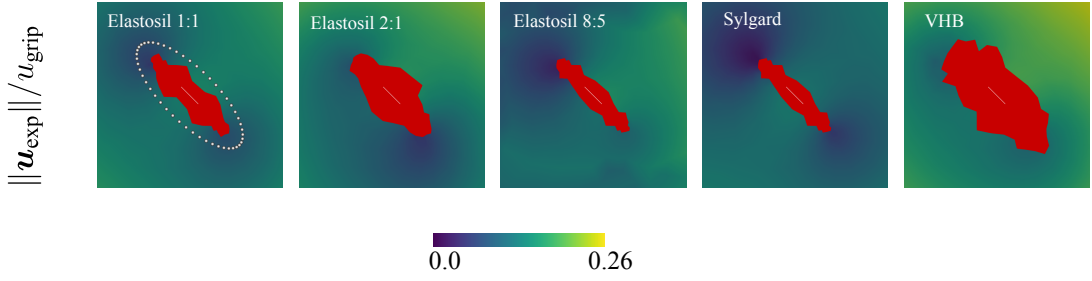
To assess the fitting accuracy of the discovered models, we compare in [Fig. 8](#) the reaction forces measured in the experiments with those predicted by the identified models. We observe that, similar to the case when Cosine similarity is used, the measured and predicted reaction forces are in good agreement.

Finally, we compare the experimentally measured displacement fields with those predicted by the identified material models. In analogy to Cosine similarity, [Fig. 9](#) shows the numerically predicted displacement fields (b) in the vicinity of the notch at the loading stage corresponding to crack onset. The experimental displacement contours (a) are consistent with those shown in [Fig. 7](#). Notably, the normalized error between experimental and predicted displacement fields (c) in [Fig. 9](#) is significantly smaller than the corresponding errors obtained using Cosine similarity in [Fig. 7c](#). This effect is particularly pronounced for Elastosil 1:1, for which the errors are almost vanishing. As discussed earlier, Cosine similarity does not account for the magnitudes of displacements. Consequently, the errors are lower when using the Euclidean similarity measure.

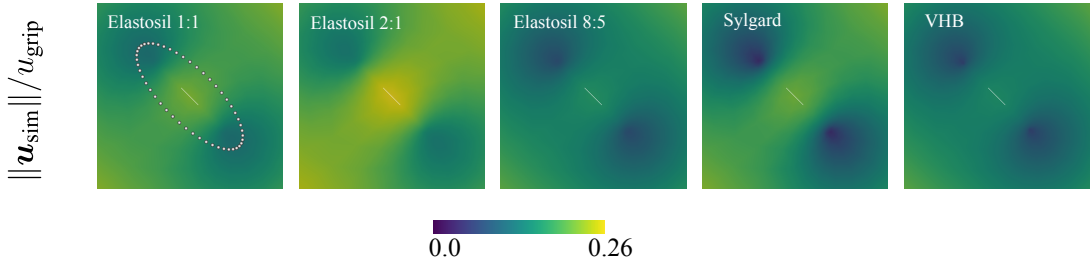
4.3. Computational time and comparison to FEMU

To assess the computational efficiency of Material Fingerprinting, we compare the runtime of its pattern recognition algorithm with that of a traditional optimization-based FEMU procedure. Assuming that the required database has already been generated or is available through an online repository, Material Fingerprinting can be performed in under one second on a standard laptop. In contrast, solving an optimization-based FEMU problem, as described in our previous work ([Moreno-Mateos et al., 2025](#)), typically requires approximately five hours. Note that these time estimations are based on the computations on a Intel® Core™ i7-13700 (13th Gen) processor. This comparison indicates that Material Fingerprinting is roughly four orders of magnitude faster. It is important to note, however, that these timings depend on the number of material parameters considered in the FEMU formulation and on the spatial discretization of the finite element simulations. Consequently, the reported speedup should be interpreted as a rough estimate of the relative computational effort.

a) Normalized experimental displacement magnitude (\mathbf{u}_{exp})



b) Numerical displacement magnitude (\mathbf{u}_{sim}) predicted by the discovered material model



c) Normalized error between numerical (\mathbf{u}_{sim}) and experimental (\mathbf{u}_{exp}) displacement magnitude

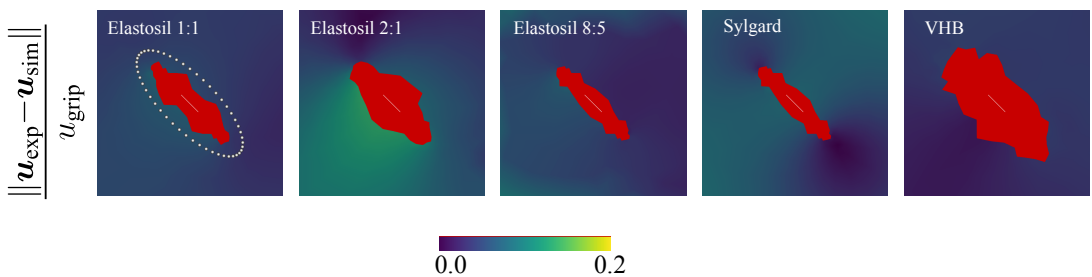


Figure 7: Normalized magnitudes of the experimental (a) and numerical (b) displacement fields in the notch vicinity for Material Fingerprinting based on Cosine similarity, obtained by dividing the displacement magnitude $\|\mathbf{u}_{\bullet}\|$ by the grip displacement right before crack onset (u_{grip}): 29.75 mm for VHB tape, 4.25 mm for Sylgard, 15.30 mm for Elastosil 2:1, 22.95 mm for Elastosil 8:5, and 21.25 mm for Elastosil 1:1. Panel (c) shows the normalized magnitude of the displacement error, computed as $\|\mathbf{u}_{\text{sim}} - \mathbf{u}_{\text{exp}}\|/u_{\text{grip}}$. The numerical predictions for each material are obtained using the corresponding material model listed in Table 1. Experimental displacement fields \mathbf{u}_{exp} were aggregated across the four experimental repetitions using the geometric mean. The chosen identification nodes are illustrated for Elastosil 1:1 as an example, but are identical for all materials. The red ellipsoidal regions near the center of the contour plots correspond to areas where DIC data is unavailable.

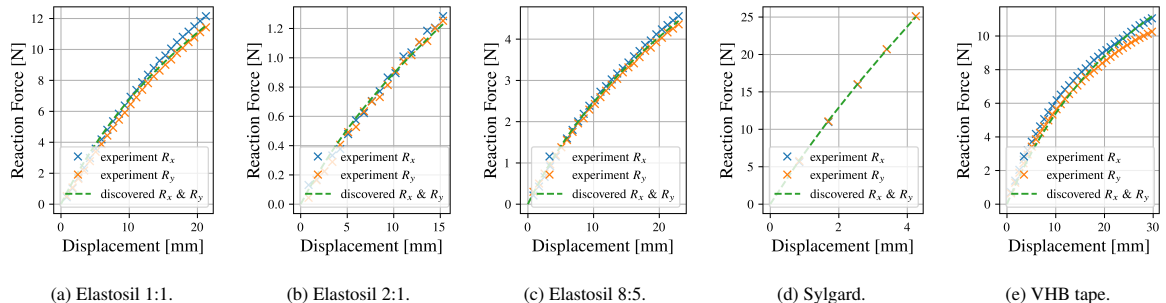


Figure 8: Comparison of the measured reaction forces and the reaction forces predicted by the discovered material models for Material Fingerprinting based on Euclidean similarity. The two reaction forces R_x and R_y are obtained from the equibiaxial experiments in [Moreno-Mateos et al. \(2025\)](#) as the measured forces on each of the two independent axes. Due to experimental variability, the two reaction forces are not exactly identical.

These results demonstrate that Material Fingerprinting offers a computationally efficient alternative to traditional FEMU, achieving inference speeds several orders of magnitude faster once an appropriate database has been constructed. While Material Fingerprinting is not intended to replace FEMU, the two approaches are complementary: Material Fingerprinting provides rapid predictions using a simplified model, whereas FEMU delivers high-fidelity

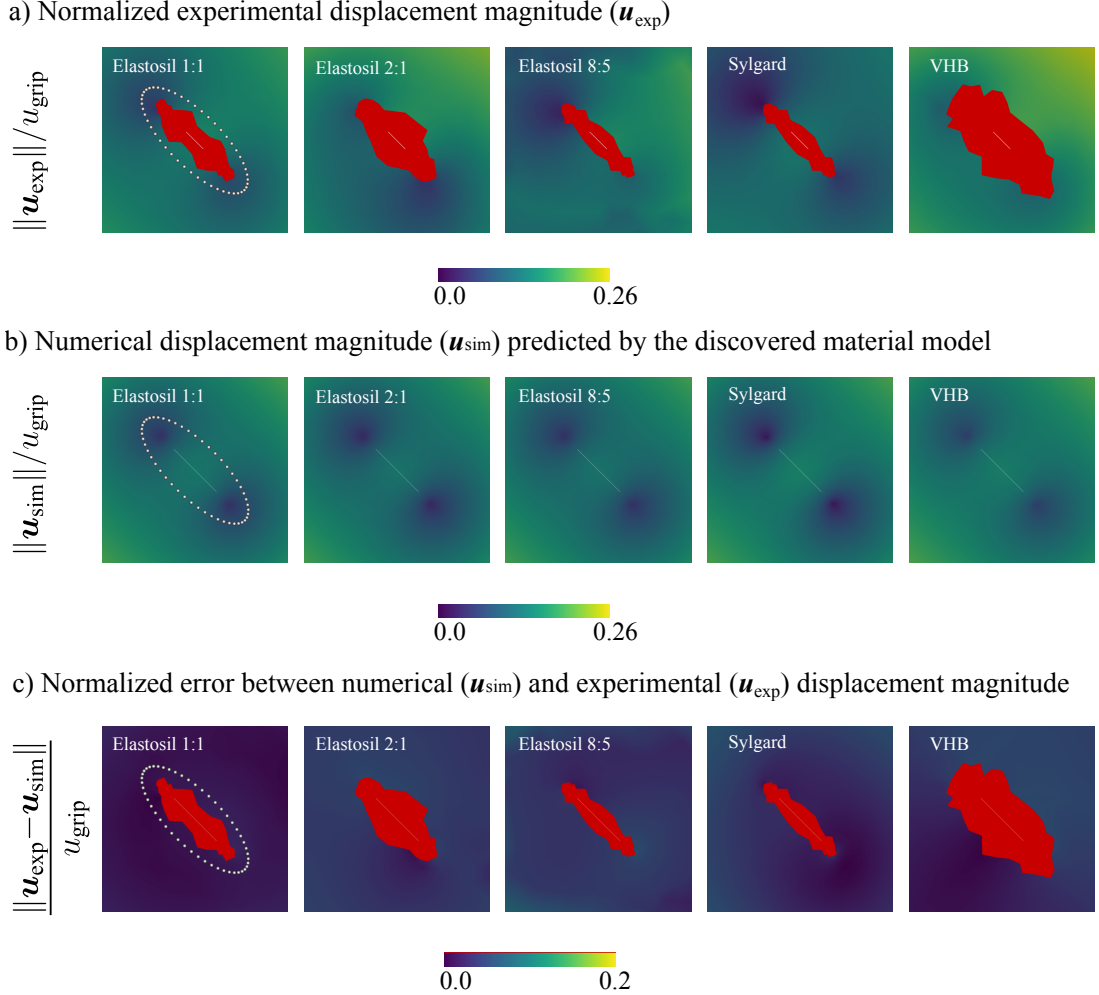


Figure 9: Normalized magnitudes of the experimental (a) and numerical (b) displacement fields in the notch vicinity for Material Fingerprinting based on Euclidean similarity, obtained by dividing the displacement magnitude $\|\mathbf{u}_{\bullet}\|$ by the grip displacement right before crack onset (u_{grip}): 29.75 mm for VHB tape, 4.25 mm for Sylgard, 15.30 mm for Elastosil 2:1, 22.95 mm for Elastosil 8:5, and 21.25 mm for Elastosil 1:1. Panel (c) shows the normalized magnitude of the displacement error, computed as $\|\mathbf{u}_{\text{sim}} - \mathbf{u}_{\text{exp}}\|/u_{\text{grip}}$. The numerical predictions for each material are obtained using the corresponding material model listed in Table 1. Experimental displacement fields \mathbf{u}_{exp} were aggregated across the four experimental repetitions using the geometric mean. The chosen identification nodes are illustrated for Elastosil 1:1 as an example, but are identical for all materials. The red ellipsoidal regions near the center of the contour plots correspond to areas where DIC data is unavailable.

results through iterative optimization. In practical settings where quick evaluations are essential, such as real-time monitoring, preliminary assessments, or large-scale parametric studies, Material Fingerprinting can be especially advantageous. Moreover, Material Fingerprinting can serve as an effective strategy for generating high-quality initial guesses that accelerate optimization-based FEMU procedures. Overall, Material Fingerprinting is a strong choice when speed and computational efficiency are prioritized, whereas FEMU remains preferable when high model accuracy is required.

5. Conclusions and outlook

In this work, we presented the first experimental validation of unsupervised Material Fingerprinting for the discovery of hyperelastic constitutive models from real full-field measurements and global reaction forces. By leveraging a precomputed database of simulated fingerprints and a pattern recognition framework, Material Fingerprinting enables ultra-fast and robust material model discovery without solving an optimization problem. The proposed approach bypasses common challenges associated with optimization-based identification techniques, including high computational cost, sensitivity to local minima, and noise amplification.

We demonstrated the effectiveness of the method using equibiaxial experiments with heterogeneous deformation fields induced by a central notch. A single database of incompressible hyperelastic material models was successfully used to characterize five distinct soft materials based solely on experimentally measured displacements and reaction forces. The identified constitutive models accurately reproduce both global force responses and local

displacement fields up to crack initiation. Moreover, we showed that, once the database is available, Material Fingerprinting achieves inference times on the order of seconds, representing a speedup of several orders of magnitude compared to traditional FEMU approaches.

Beyond validating unsupervised Material Fingerprinting on experimental data, we introduced and assessed two similarity measures for fingerprint matching. While Cosine similarity emphasizes the shape of the fingerprints, a Euclidean-distance-based metric preserves information about both shape and magnitude and is particularly well suited for fingerprints that combine heterogeneous physical quantities. Both approaches yielded consistent and physically interpretable results, which highlight the robustness and flexibility of the Material Fingerprinting framework.

The present study focuses on isotropic, incompressible hyperelastic materials under quasi-static loading. Future work will aim to expand the database to include more complex material behaviors, such as anisotropy, compressibility, and rate-dependent or dissipative effects. Likewise, alternative experiments for unsupervised material fingerprinting may include compression-based setups such as indentation of soft materials ([Moreno-Mateos and Steinmann, 2026](#)). In addition, incorporating uncertainty quantification, adaptive database refinement, and hybrid strategies that combine Material Fingerprinting with optimization-based methods, for example, by using Material Fingerprinting to provide high-quality initial guesses for FEMU, represents a promising direction.

Code and data availability

The code and data are publicly available on GitHub:

<https://github.com/orgs/Material-Fingerprinting/>

We acknowledge the use of the dolfiny implementation of principal stretch computations and their derivatives:

<https://github.com/fenics-dolfiny/dolfiny>

Acknowledgments

The authors acknowledge support from the European Research Council (ERC) under the Horizon Europe Program, Grant-No. 101141626 DISCOVER and Grant-No. 101052785 SoftFrac. Funded by the European Union. Views and opinions expressed are, however, those of the authors only and do not necessarily reflect those of the European Union or the European Research Council Executive Agency. Neither the European Union nor the granting authority can be held responsible for them.



Appendix A. Finite element implementation of forward simulations

In the absence of traction and body forces, the weak form of the forward simulations to generate the database reads

$$\int_{\mathcal{B}_0} [[\partial_F \tilde{W} - p J F^{-T}] : \nabla_0 \delta \mathbf{u} - [J - 1] \delta p] \, dV = 0, \quad (\text{A.1})$$

where $\delta \mathbf{u}$ and δp are test functions, and \mathcal{B}_0 is the integration domain in the material configuration.

The open-source finite element platform FEniCSx version 0.9.0 ([Baratta et al., 2023](#)) is used to solve the weak form of the problem with a continuous Galerkin discretization of trial and test functions consisting of quadratic Lagrange polynomial basis functions for the displacement field and linear Lagrange polynomial basis functions for the pressure field (Taylor-Hood element). We use the library `uf1.diff` to compute $\partial_F \tilde{W}$ via symbolic differentiation. The finite element mesh has 1016 nodes, 2857 tetrahedra elements, and it mimics half the thickness of the sample and the displacement is fixed to zero on the middle-thickness symmetry plane.

Appendix B. Experimental fingerprint measurement

As described previously, the fingerprints contain both reaction forces and displacements across multiple load steps. The raw experimental measurements must therefore be preprocessed to construct the experimental fingerprint. Specifically, the displacement fields obtained via DIC are downsampled to a predefined set of identification nodes located on an ellipse surrounding the initial notch (Figs. 2 and 3). The Resample With Dataset filter in ParaView is employed for this purpose, using as inputs the raw DIC measurements (coordinates and displacement values) and the coordinates of the ellipse points. In this work, $n_u = 50$ identification points were defined along the ellipse. The resampling is performed independently for each considered load step (clamp loading stage), displacement component (horizontal and vertical), and experimental repetition. Subsequently, the geometric mean across four experimental repetitions is computed at each identification point and load step. The resulting horizontal and vertical displacement components are then flattened across load steps and identification points to form the experimental displacement fingerprint vector f_u .

The construction of the experimental force fingerprint vector f_R requires less preprocessing. Using the mapping between load-step indices and prescribed clamp displacements, the raw experimental force-displacement curves are evaluated at the desired load steps. When no data point is available exactly at a prescribed clamp displacement, the corresponding force value is obtained by linear interpolation along the experimental force-displacement curve. Analogously to the displacements, the (interpolated) forces in the horizontal and vertical directions are flattened across load steps to form f_R .

References

Abdusalamov, R., Hillgärtner, M., Itskov, M., 2023. Automatic generation of interpretable hyperelastic material models by symbolic regression. *International Journal for Numerical Methods in Engineering*, nme.7203URL: <https://onlinelibrary.wiley.com/doi/10.1002/nme.7203>, doi:10.1002/nme.7203.

As'ad, F., Farhat, C., 2022. A Mechanics-Informed Neural Network Framework for Data-Driven Nonlinear Viscoelasticity URL: <https://rgdoi.net/10.13140/RG.2.2.21694.36168>, doi:10.13140/RG.2.2.21694.36168. publisher: Unpublished.

Avril, S., Bonnet, M., Bretelle, A.S., Grédiac, M., Hild, F., Ienny, P., Latourte, F., Lemosse, D., Pagano, S., Pagnacco, E., Pierron, F., 2008. Overview of Identification Methods of Mechanical Parameters Based on Full-field Measurements. *Experimental Mechanics* 48, 381–402. URL: <http://link.springer.com/10.1007/s11340-008-9148-y>, doi:10.1007/s11340-008-9148-y.

Baratta, I.A., Dean, J.P., Dokken, J.S., Habera, M., Hale, J.S., Richardson, C.N., Rognes, M.E., Scroggs, M.W., Sime, N., Wells, G.N., 2023. Dolfinx: The next generation fenics problem solving environment. URL: <https://doi.org/10.5281/zenodo.10447666>, doi:10.5281/zenodo.10447666.

Bleyer, J., 2025. Learning elastoplasticity with implicit layers doi:<http://dx.doi.org/10.2139/ssrn.5210734>.

Carroll, M.M., 2011. A Strain Energy Function for Vulcanized Rubbers. *Journal of Elasticity* 103, 173–187. URL: <http://link.springer.com/10.1007/s10659-010-9279-0>, doi:10.1007/s10659-010-9279-0.

Claire, D., Hild, F., Roux, S., 2004. A finite element formulation to identify damage fields: the equilibrium gap method. *International Journal for Numerical Methods in Engineering* 61, 189–208. URL: <https://onlinelibrary.wiley.com/doi/10.1002/nme.1057>, doi:10.1002/nme.1057.

Collins, J.D., Hart, G.C., Hasselman, T.K., Kennedy, B., 1974. Statistical identification of structures. <https://doi.org/10.2514/3.49190> 12, 185–190. URL: <https://arc.aiaa.org/doi/10.2514/3.49190>, doi:10.2514/3.49190.

Dal, H., Açıkgöz, K., Badienia, Y., 2021. On the Performance of Isotropic Hyperelastic Constitutive Models for Rubber-Like Materials: A State of the Art Review. *Applied Mechanics Reviews* 73, 020802. URL: <https://asmedigitalcollection.asme.org/appliedmechanicsreviews/article/73/2/020802/1108153/On-the-Performance-of-Isotropic-Hyperelastic>, doi:10.1115/1.4050978.

Davies, M., Puy, G., Vandergheynst, P., Wiaux, Y., 2014. A Compressed Sensing Framework for Magnetic Resonance Fingerprinting. URL: <http://arxiv.org/abs/1312.2465>. arXiv:1312.2465 [cs, math].

Dong, G., Flaschel, M., Hintermüller, M., Papafitsoros, K., Sirotenko, C., Tabelow, K., 2025. Data-driven methods for quantitative imaging. *GAMM-Mitteilungen* 48, e202470014. URL: <https://onlinelibrary.wiley.com/doi/10.1002/gamm.202470014>, doi:10.1002/gamm.202470014.

Filip, J., Dechterenko, F., Schmidt, F., Lukavsky, J., Vilimovska, V., Kotera, J., Fleming, R.W., 2024. Material Fingerprinting: Identifying and Predicting Perceptual Attributes of Material Appearance. URL: <http://arxiv.org/abs/2410.13615>, doi:10.48550/arXiv.2410.13615. arXiv:2410.13615 [cs].

Flaschel, M., Hastie, T., Kuhl, E., 2025a. Non-smooth optimization meets automated material model discovery. URL: <http://arxiv.org/abs/2507.10196>, doi:10.48550/arXiv.2507.10196. arXiv:2507.10196 [cs].

Flaschel, M., Kumar, S., De Lorenzis, L., 2021. Unsupervised discovery of interpretable hyperelastic constitutive laws. *Computer Methods in Applied Mechanics and Engineering* 381, 113852. doi:10.1016/j.cma.2021.113852.

Flaschel, M., Kumar, S., De Lorenzis, L., 2022. Discovering plasticity models without stress data. *npj Computational Materials* 8, 91. URL: <https://www.nature.com/articles/s41524-022-00752-4>, doi:10.1038/s41524-022-00752-4.

Flaschel, M., Kumar, S., De Lorenzis, L., 2023. Automated discovery of generalized standard material models with EUCLID. *Computer Methods in Applied Mechanics and Engineering* 405, 115867. URL: <https://linkinghub.elsevier.com/retrieve/pii/S0045782522008234>, doi:10.1016/j.cma.2022.115867.

Flaschel, M., Martonová, D., Veil, C., Kuhl, E., 2025b. Python package for Material Fingerprinting. Zenodo doi:<http://doi.org/10.5281/zenodo.17098250>.

Flaschel, M., Martonová, D., Veil, C., Kuhl, E., 2026. Material Fingerprinting: A shortcut to material model discovery without solving optimization problems. *Computer Methods in Applied Mechanics and Engineering* 450, 118573. URL: <https://linkinghub.elsevier.com/retrieve/pii/S004578252500845X>, doi:10.1016/j.cma.2025.118573.

Flaschel, M., Steinmann, P., De Lorenzis, L., Kuhl, E., 2025c. Convex neural networks learn generalized standard material models. *Journal of the Mechanics and Physics of Solids* 200, 106103. URL: <https://linkinghub.elsevier.com/retrieve/pii/S0022509625000791>, doi:10.1016/j.jmps.2025.106103.

Frankel, A.L., Jones, R.E., Swiler, L.P., 2020. TENSOR BASIS GAUSSIAN PROCESS MODELS OF HYPERELASTIC MATERIALS. *Journal of Machine Learning for Modeling and Computing* 1, 1–17. URL: <http://www.dl.begellhouse.com/journals/558048804a15188a,583c4e56625ba94e,651a2e6b0260f708.html>, doi:10.1615/JMachLearnModelComput.2020033325.

Fuhg, J.N., Anantha Padmanabha, G., Bouklas, N., Bahmani, B., Sun, W., Vlassis, N.N., Flaschel, M., Carrara, P., De Lorenzis, L., 2024. A Review on Data-Driven Constitutive Laws for Solids. *Archives of Computational Methods in Engineering* URL: <https://link.springer.com/10.1007/s11831-024-10196-2>, doi:10.1007/s11831-024-10196-2.

Fuhg, J.N., Marino, M., Bouklas, N., 2022. Local approximate Gaussian process regression for data-driven constitutive models: development and comparison with neural networks. *Computer Methods in Applied Mechanics and Engineering* 388, 114217. URL: <https://linkinghub.elsevier.com/retrieve/pii/S004578252100548X>, doi:10.1016/j.cma.2021.114217.

Geubelle, P.H., Knauss, W.G., 1994. Finite strains at the tip of a crack in a sheet of hyperelastic material: I. Homogeneous case. *Journal of Elasticity* 35, 61–98. URL: <http://link.springer.com/10.1007/BF00115539>, doi:10.1007/BF00115539.

Geuken, G.L., Kurzeja, P., Wiedemann, D., Mosler, J., 2025. Input convex neural networks: universal approximation theorem and implementation for isotropic polyconvex hyperelastic energies. URL: <http://arxiv.org/abs/2502.08534>, doi:10.48550/arXiv.2502.08534. arXiv:2502.08534 [cs].

Ghaboussi, J., Garrett, J.H., Wu, X., 1991. Knowledge-Based Modeling of Material Behavior with Neural Networks. *Journal of Engineering Mechanics* 117, 132–153. URL: <http://ascelibrary.org/doi/10.1061/%28ASCE%290733-9399%281991%29117%3A1%28132%29>, doi:10.1061/(ASCE)0733-9399(1991)117:1(132).

Grédiac, M., 1989. Principle of virtual work and identification. *Comptes Rendus de L Academie des Sciences Serie Ii* , 1–5.

Grédiac, M., Pierron, F., Avril, S., Toussaint, E., 2006. The virtual fields method for extracting constitutive parameters from full-field measurements: a review. *Strain* 42, 233–253. URL: <https://onlinelibrary.wiley.com/doi/full/10.1111/j.1475-1305.2006.tb01504.x> <https://onlinelibrary.wiley.com/doi/10.1111/j.1475-1305.2006.tb01504.x>, doi:10.1111/J.1475-1305.2006.TB01504.X.

Grédiac, M., Vautrin, A., 1990. A new method for determination of bending rigidities of thin anisotropic plates. *Journal of Applied Mechanics* 57, 964–968. doi:10.1115/1.2897668.

Ibañez, R., Borzacchiello, D., Aguado, J.V., Abisset-Chavanne, E., Cueto, E., Ladeveze, P., Chinesta, F., 2017. Data-driven non-linear elasticity: constitutive manifold construction and problem discretization. *Computational Mechanics* 60, 813–826. URL: <http://link.springer.com/10.1007/s00466-017-1440-1>, doi:10.1007/s00466-017-1440-1.

Jaafreh, R., Kumar, S., Hamad, K., Kim, J.G., 2025. Introducing Materials Fingerprint (MatPrint): A novel method in graphical material representation and features compression. *Computational Materials Science* 246, 113444. URL: <https://linkinghub.elsevier.com/retrieve/pii/S0927025624006657>, doi:10.1016/j.commatsci.2024.113444.

Kalina, K.A., Brummund, J., Sun, W., Kästner, M., 2025. Neural networks meet anisotropic hyperelasticity: A framework based on generalized structure tensors and isotropic tensor functions. *Computer Methods in Applied Mechanics and Engineering* 437, 117725. URL: <https://linkinghub.elsevier.com/retrieve/pii/S0045782524009812>, doi:10.1016/j.cma.2024.117725.

Kirchdoerfer, T., Ortiz, M., 2016. Data-driven computational mechanics. *Computer Methods in Applied Mechanics and Engineering* 304, 81–101. URL: <https://linkinghub.elsevier.com/retrieve/pii/S0045782516300238>, doi:10.1016/j.cma.2016.02.001.

Klein, D.K., 2025. Polyconvex Hyperelasticity with Neural Networks: On Invariant- and Coordinate-Based Models, Benefits and Limitations. Ph.D. thesis. Universitäts- und Landesbibliothek Darmstadt. URL: <https://tuprints.ulb.tu-darmstadt.de/handle/tuda/14802>, doi:10.26083/TUDA-7577.

Klein, D.K., Fernández, M., Martin, R.J., Neff, P., Weeger, O., 2022. Polyconvex anisotropic hyperelasticity with neural networks. *Journal of the Mechanics and Physics of Solids* 159, 104703. URL: <https://linkinghub.elsevier.com/retrieve/pii/S0022509621003215>, doi:10.1016/j.jmps.2021.104703.

Kuban, M., Gabaj, S., Aggoune, W., Vona, C., Rigamonti, S., Draxl, C., 2022. Similarity of materials and data-quality assessment by fingerprinting. *MRS Bulletin* 47, 991–999. URL: <https://link.springer.com/10.1557/s43577-022-00339-w>, doi:10.1557/s43577-022-00339-w.

Linden, L., Klein, D.K., Kalina, K.A., Brummund, J., Weeger, O., Kästner, M., 2023. Neural networks meet hyperelasticity: A guide to enforcing physics. *Journal of the Mechanics and Physics of Solids* 179, 105363. URL: <https://linkinghub.elsevier.com/retrieve/pii/S0022509623001679>, doi:10.1016/j.jmps.2023.105363.

Linka, K., Kuhl, E., 2023. A new family of Constitutive Artificial Neural Networks towards automated model discovery. *Computer Methods in Applied Mechanics and Engineering* 403, 115731. URL: <https://linkinghub.elsevier.com/retrieve/pii/S0045782522006867>, doi:10.1016/j.cma.2022.115731.

Linka, K., Kuhl, E., 2024. Best-in-class modeling: A novel strategy to discover constitutive models for soft matter systems. *Extreme Mechanics Letters* 70, 102181. URL: <https://linkinghub.elsevier.com/retrieve/pii/S2352431624000610>, doi:10.1016/j.eml.2024.102181.

Lopez-Pamies, O., 2009. A new I₁-based hyperelastic model for rubber elastic materials. *Comptes Rendus. Mécanique* 338, 3–11. URL: <https://comptes-rendus.academie-sciences.fr/mecanique/articles/10.1016/j.crme.2009.12.007/>, doi:10.1016/j.crme.2009.12.007.

Ma, D., Gulani, V., Seiberlich, N., Liu, K., Sunshine, J.L., Duerk, J.L., Griswold, M.A., 2013. Magnetic resonance fingerprinting. *Nature* 495, 187–192. URL: <http://www.nature.com/articles/nature11971>, doi:10.1038/nature11971.

Martonová, D., Kuhl, E., Flaschel, M., 2026. Material Fingerprinting for rapid discovery of hyperelastic models: First experimental validation. *Journal of the Mechanics and Physics of Solids* 208, 106463. URL: <https://linkinghub.elsevier.com/retrieve/pii/S0022509625004375>, doi:10.1016/j.jmps.2025.106463.

Masi, F., Stefanou, I., 2023. Evolution TANN and the identification of internal variables and evolution equations in solid mechanics. *Journal of the Mechanics and Physics of Solids* 174, 105245. URL: <https://linkinghub.elsevier.com/retrieve/pii/S0022509623000492>, doi:10.1016/j.jmps.2023.105245.

McGivney, D.F., Pierre, E., Ma, D., Jiang, Y., Saybasili, H., Gulani, V., Griswold, M.A., 2014. SVD Compression for Magnetic Resonance Fingerprinting in the Time Domain. *IEEE Transactions on Medical Imaging* 33, 2311–2322. URL: <https://ieeexplore.ieee.org/document/6851901>, doi:10.1109/TMI.2014.2337321.

Moreno-Mateos, M.A., Steinmann, P., 2026. Cutting soft materials: how material differences shape the response. *npj Computational Materials* 12, 15. URL: <https://www.nature.com/articles/s41524-025-01869-y>, doi:10.1038/s41524-025-01869-y.

Moreno-Mateos, M.A., Wiesheier, S., Esmaeili, A., Hossain, M., Steinmann, P., 2025. Biaxial characterization of soft elastomers: Experiments and data-adaptive configurational forces for fracture. *Journal of the Mechanics and Physics of Solids* 205, 106339. URL: <https://linkinghub.elsevier.com/retrieve/pii/S0022509625003138>, doi:10.1016/j.jmps.2025.106339.

Ogden, R.W., 1972. Large deformation isotropic elasticity – on the correlation of theory and experiment for incompressible rubberlike solids. *Proceedings of the Royal Society of London. Series A, Mathematical and Physical Sciences*, , 565–584.

Pierron, F., Grédiac, M., 2020. Towards Material Testing 2.0. A review of test design for identification of constitutive parameters from full-field measurements. *Strain* URL: <https://onlinelibrary.wiley.com/doi/10.1111/str.12370>, doi:10.1111/str.12370.

Rivlin, 1950. Large elastic deformations of isotropic materials. I. Fundamental concepts , 32.

Rosenkranz, M., Kalina, K.A., Brummund, J., Kästner, M., 2023. A comparative study on different neural network architectures to model inelasticity. *International Journal for Numerical Methods in Engineering* 124, 4802–4840. URL: <https://onlinelibrary.wiley.com/doi/10.1002/nme.7319>, doi:10.1002/nme.7319.

Rouze, N.C., Deng, Y., Trutna, C.A., Palmeri, M.L., Nightingale, K.R., 2018. Characterization of Viscoelastic Materials Using Group Shear Wave Speeds. *IEEE Transactions on Ultrasonics, Ferroelectrics, and Frequency Control* 65, 780–794. URL: <https://ieeexplore.ieee.org/document/8314723/>, doi:10.1109/TUFFC.2018.2815505.

Römer, U., Hartmann, S., Tröger, J.A., Anton, D., Wessels, H., Flaschel, M., De Lorenzis, L., 2025. Reduced and All-At-Once Approaches for Model Calibration and Discovery in Computational Solid Mechanics. *Applied Mechanics Reviews* 77, 040801. URL: <https://asmedigitalcollection.asme.org/appliedmechanicsreviews/article/77/4/040801/1201974/Reduced-and-All-At-Once-Approaches-for-Model>, doi:10.1115/1.4066118.

Schoenauer, M., Sebag, M., Jouve, F., Lamy, B., Maitournam, H., 1996. Evolutionary identification of macro-mechanical models. *Advances in Genetic Programming II* , 467–488.

Spannaus, A., Law, K.J., Luszczek, P., Nasrin, F., Micucci, C.P., Liaw, P.K., Santodonato, L.J., Keffer, D.J., Maroulas, V., 2021. Materials Fingerprinting Classification. *Computer Physics Communications* 266, 108019. URL: <https://linkinghub.elsevier.com/retrieve/pii/S0010465521001314>, doi:10.1016/j.cpc.2021.108019.

Stephenson, R.A., 1982. The equilibrium field near the tip of a crack for finite plane strain of incompressible elastic materials. *Journal of Elasticity* 12, 65–99. URL: <http://link.springer.com/10.1007/BF00043706>, doi:10.1007/BF00043706.

Sussman, T., Bathe, K.J., 2009. A model of incompressible isotropic hyperelastic material behavior using spline interpolations of tension-compression test data. *Communications in Numerical Methods in Engineering* 25, 53–63. URL: <http://doi.wiley.com/10.1002/cnm.1105>, doi:10.1002/cnm.1105.

Tac, V., Sahli Costabal, F., Tepole, A.B., 2022. Data-driven tissue mechanics with polyconvex neural ordinary differential equations. *Computer Methods in Applied Mechanics and Engineering* 398, 115248. URL: <https://linkinghub.elsevier.com/retrieve/pii/S0045782522003838>, doi:10.1016/j.cma.2022.115248.

Tacke, M., Busch, M., Bali, K., Abdolazizi, K., Linka, K., Cyron, C., Aydin, R., 2025. Constitutive scientific generative agent (CSGA): Leveraging large language models for automated constitutive model discovery. *Machine Learning for Computational Science and Engineering* 1, 23. URL: <https://link.springer.com/10.1007/s44379-025-00022-2>, doi:10.1007/s44379-025-00022-2.

Treloar, L.R.G., 1944. Stress-strain data for vulcanised rubber under various types of deformation. *Transactions of the Faraday Society* 40, 59. URL: <http://xlink.rsc.org/?DOI=tf9444000059>, doi:10.1039/tf9444000059.

Trutna, C.A., Knight, A.E., Rouze, N.C., Hobson-Webb, L.D., Palmeri, M.L., Nightingale, K.R., 2020a. Viscoelastic Characterization in Muscle using Group Speed Analysis and Volumetric Shear Wave Elasticity Imaging, in: 2020 IEEE International Ultrasonics Symposium (IUS), IEEE, Las Vegas, NV, USA. pp. 1–4. URL: <https://ieeexplore.ieee.org/document/9251751/>, doi:10.1109/IUS46767.2020.9251751.

Trutna, C.A., Rouze, N.C., Palmeri, M.L., Nightingale, K.R., 2019. Robust Model-Based Viscoelastic Characterization of QIBA Phantoms through Fractional Derivative Group Shear Wave Speeds, in: 2019 IEEE International Ultrasonics Symposium (IUS), IEEE, Glasgow, United Kingdom. pp. 1391–1394. URL: <https://ieeexplore.ieee.org/document/8925625/>, doi:10.1109/ULTSYM.2019.8925625.

Trutna, C.A., Rouze, N.C., Palmeri, M.L., Nightingale, K.R., 2020b. Measurement of Viscoelastic Material Model Parameters Using Fractional Derivative Group Shear Wave Speeds in Simulation and Phantom Data. *IEEE Transactions on Ultrasonics, Ferroelectrics, and Frequency Control* 67, 286–295. URL: <https://ieeexplore.ieee.org/document/8850040/>, doi:10.1109/TUFFC.2019.2944126.

Urrea-Quintero, J., Anton, D., De Lorenzis, L., Wessels, H., 2026. Automated constitutive model discovery by pairing sparse regression algorithms with model selection criteria. *Computer Methods in Applied Mechanics and Engineering* 449, 118551. URL: <https://linkinghub.elsevier.com/retrieve/pii/S0045782525008230>, doi:10.1016/j.cma.2025.118551.

Wiesheier, S., Moreno-Mateos, M.A., Steinmann, P., 2024. Versatile data-adaptive hyperelastic energy functions for soft materials. *Computer Methods in Applied Mechanics and Engineering* 430, 117208. URL: <https://linkinghub.elsevier.com/retrieve/pii/S004578252400464X>, doi:10.1016/j.cma.2024.117208.

Wiesheier, S., Moreno-Mateos, M.A., Steinmann, P., 2026. Data-adaptive spline-based viscoelasticity for soft solids. *Computer Methods in Applied Mechanics and Engineering* 451, 118705. URL: <https://linkinghub.elsevier.com/retrieve/pii/S0045782525009776>, doi:10.1016/j.cma.2025.118705.

Yeoh, O.H., 1990. Characterization of elastic properties of carbon-black-filled rubber vulcanizates. *Rubber chemistry and technology* 63, 792–805.